Additive Manufacturing Letters 11 (2024) 100253

Contents lists available at ScienceDirect

Additive Manufacturing Letters

journal homepage: www.elsevier.com/locate/addlet

Short communication

Understanding the effect of pre-sintering scanning strategy on the relative density of Zr-modified Al7075 processed by laser powder bed fusion

Nicolas Nothomb [a,*], Ignacio Rodriguez-Barber [b], María Teresa Pérez-Prado [b], Norberto Jimenez Mena [c], Grzegorz Pyka [a], Aude Simar [a]

[a] UCLouvain, IMMC (Institute of Mechanics, Materials and Civil Engineering), Louvain-la-Neuve, Belgium
[b] IMDEA Materials Institute, Calle Eric Kandel, 2, 28906, Getafe, Madrid, Spain
[c] CRM group, Avenue du bois St. Jean 21, 4000, Liège, Belgium

ARTICLE INFO

Keywords:
Additive manufacturing
L-PBF
Al7075
Pre-sintering

ABSTRACT

Only a limited aluminium material palette is currently available for L-PBF processing, especially for high strength aluminium alloy. Unmodified Al7075 suffers from hot cracking making it nearly impossible to process by L-PBF. Adding some grain refiner to Al7075 solves this issue of hot cracking. However, this alloy still presents difficulties to be processed with densities above 99.5%. In this study, the unconventional pre-sintering scanning strategy is applied to process 99.9% density Al7075+1.8%Zr. For this scanning strategy, each layer is scanned twice with different power, i.e. it is first scanned with half the power selected for the second scan. This specific strategy remelts potential defect generated by the first scan and reduces lack of fusion pores. These two phenomena lead to high density L-PBF Al7075+1.8%Zr and pave the way to higher densities for high strength aluminium alloys.

1. Introduction

Additive manufacturing (AM) is no longer restricted to rapid prototyping. Nowadays, the aerospace, medical, energy and automotive industries have a continuously growing demand for high performance complex metal parts [1,2]. For aluminium alloys, laser powder bed fusion (L-PBF) is the leading AM technology. It allows processing complex parts with high resolution and surface finish but L-PBF is currently restricted to a small building volume [3,4]. This manufacturing technique is characterised by a higher cooling rate than conventional manufacturing methods (between 10^3 and 10^8 K/s) and imposes multiple thermal cycles to the material. This innovative process generates unique, complex and interesting microstructures that can lead to outstanding mechanical properties [1,5,6]. Due to complex processing conditions, each new material requires an extensive amount of research to find the optimised set of parameters that allows the building of fully dense parts with the desired properties. Moreover, only a limited commercially available material palette is able to sustain easily these extreme processing conditions [1,3].

AlSi10Mg and AlSi12 are the most extensively studied L-PBF aluminum alloys [7–13]. These alloys initially designed for casting exhibit a low solidification range and form large fraction of eutectic phase at the end of solidification [14]. Thus, they can easily sustain the high cooling rate making dense parts relatively easy to process. However they do not ensure high mechanical performances: their yield strength is usually between 200 and 300 MPa [8,11,13]. Unlike the mentioned two alloys, the processing of high strength aluminium alloys suffers from several inherent issues when processed by L-PBF, including hot cracking due to their large solidification interval [2,3,6,15] and loss of alloying elements (Zn and Mg) during processing due to preferential evaporation [2,3]. Research on process parameter optimisation has, to date, not rendered good results in terms of eliminating hot cracking in unmodified 7xxx series alloys [16–19].

To allow L-PBF processing of high strength aluminium, the most widespread solution is adding a grain refiner to the alloy. In 2017, Martin et al. [20] coated Al7075 powder with small micron sized Zr particles. As a result, sub-micron Al_3Zr precipitates are formed at the beginning of solidification. They will act as preferential nucleation sites for aluminium grains and thereby transform the classical columnar microstructure generated by L-PBF into one composed of fine equiaxed grains [20]. This new refined microstructure is free of hot cracking due to a better distribution of the solidification strains as well as a better liquid feeding in the latest stages of solidification [21]. Zr is an efficient grain refiner due to its low lattice mismatch with aluminium combined with the early formation of sub-micron Al_3Zr precipitates. These two characteristics allow the aluminium phase to nucleate preferentially on

* Corresponding author.
E-mail address: nicolas.nothomb@uclouvain.be (N. Nothomb).

https://doi.org/10.1016/j.addlet.2024.100253
Received 15 April 2024; Received in revised form 20 October 2024; Accepted 30 October 2024
Available online 13 November 2024

coherent precipitates formed at the onset of solidification. Following this seminal work, Zr became frequently selected for processing a wide range of high strength aluminium alloys using L-PBF [22–33] as proposed in the present study.

L-PBF processed Al alloys are often targeted for applications in the aerospace sector, which require an outstanding fatigue performance. For fatigue properties to meet industry demands, porosity must be minimised, especially the fraction of pores larger than 50 μm [9]. The current lack of literature about fatigue properties of L-PBF Al 7xxx series could be explained by the high Zn and Mg preferential evaporation that make high relative density complex to reach. Indeed, these two elements suffer from a high vapour pressure [34] which leads to their loss during manufacturing [20,30,35,36]. Evaporation also generates spatters [37] and gas pores [8,30,38]. Therefore, most relative density values reported in the literature lie below 99.5% [31,36,39–41] while only few works report higher densities (with 99.8% as the best density reported) [35,42–44]. The origin of such high density values has not been properly explained. Thus there is a need to understand deeply how to reach these kind of high densities to aim for better mechanical properties.

A solution used only twice in literature to improve density of L-PBF aluminium alloys is the use of pre-sintering (PS) scanning strategy. Aboulkhair et al. [7] successfully reached 99.8% density in L-PBF AlSi10Mg by scanning each layer twice: first with a power of 50 W and afterwards with a power of 100 W while keeping the other scanning parameters constant. Xie et al. [45] confirmed that using a higher power second scan helps removing defects left by the first scan in the case of L-PBF Ti6Al4V. The beneficial effect of a first low power scan to reduce porosity was confirmed for L-PBF AlSi10Mg by Weingarten et al. [46] using a laser drying of the powder using an even lower power first scan (first scan = 50 W, second scan = 910 W). In their case, it could not really be considered as PS since the first laser pass does not melt the powder. This promising PS scanning strategy remains unexplored for high-strength L-PBF aluminium alloys.

Hence, the main objective of this work is to successfully process fully dense Al7075 parts by L-PBF that are free of hot cracking. ZrH_2 was added to the pre-alloyed powder to avoid hot cracking and an unconventional PS strategy was used to reach a relative density above 99.5%. To understand deeply the effect of this unconventional scanning strategy on the specific case of Al7075, microstructural characterisation by electron backscattered diffraction (EBSD) and optical micrography (OM) combined with microfocus X-ray computed tomography was performed. This work paves the way to a detailed characterisation of static and dynamic mechanical performances on this promising high-strength L-PBF aluminium alloy.

2. Materials and methods

2.1. Powder feedstock

Two different powder feedstocks will be used in this work. The first one is a pre-alloyed Al7075 powder (Carpenter Additive, UK) without any addition. The second one is a mechanical mix of the same pre-alloyed Al7075 powder with ZrH_2 (Nanografi, Turkey). The two powders are mechanically mixed together using a turbula mixer for at least six hours. The particle size distribution (PSD) of the Al7075 is characterised by d_{10} = 21 μm, d_{50} = 38 μm and d_{90} = 63 μm while for the ZrH_2 it is d_{10} = 3 μm, d_{50} = 14 μm and d_{90} = 36 μm. These PSD were obtained by wet sieving of the powder and a measurement by laser diffraction using a Coulter LS 100Q equipment. The complete PSD is available in supplementary Figure A.1. Inductively coupled plasma optical emission spectroscopy (ICP-OES) analyses were performed on the powder mix. Samples were dissolved before being analysed using an Agilient Technologies 5100 ICP-OES. The chemical composition obtained using these analyses is reported in Table 1. The powder mix will thus be called Al7075+1.8wt%Zr throughout this article. ICP analyses were also performed on solid L-PBF samples (see Table 1).

Powders and L-PBF samples were also analysed using an Oxygen/Nitrogen/Hydrogen Elemental Analyser (ONH836, LECO). It allows to have access to the total amount of H by inert gas fusion of the samples, which is not possible using ICP-OES.

2.2. L-PBF process

A ProX®DMP 200 system (3D Systems Inc., USA) was used to process the Al7075 and Al7075+1.8%Zr alloys. The laser is operated at a 1075 nm wavelength, a 70 μm spot size and with a maximum power of 273 W. The samples were manufactured on a non-heated squared Al5Mg (wt%Mg) build-plate of size 141 mm × 141 mm. Processing of rectangular parallelepipeds of size 10 mm × 10 mm × 5 mm was performed under argon gas keeping the chamber below 500 ppm of O_2.

Concerning the processing parameters, the layer thickness (t) was kept constant at 30 μm. Two scanning strategies are compared. In the first one, called single scan (SS), the scanning pattern is composed of 5000 μm side regular hexagon with 100 μm overlapping between adjacent hexagons. Within each hexagon, a meander scanning strategy is used. Between each layer, a rotation of 90° is applied on the scanning pattern. Initially, a wide range of power (P)(109 W–273 W) and scanning speed (v)(100 mm/s–2000 mm/s) combined with a fixed hatching space (HS) of 100 μm were tested to find an optimum set of parameters. The HS was also modified between 50 μm and 295 μm without significantly improving the density. The SS strategy is compared to the pre-sintering (PS) scanning strategy was utilised. In the PS strategy, each layer is scanned twice, the first time with half the power of the second scan. To the author's knowledge, PS was only used twice in literature (see Section 1). A complete list of the parameters tested in this study is available in the supplementary material: in Table A.1 for Al7075 and Table A.2 for Al7075+1.8%Zr.

2.3. Characterisation

The porosity of the manufactured parallelepipeds was analysed using three complementary characterisation techniques. To allow a fast and effective screening of the numerous process parameters analysed, the Archimedes method was utilised in ethanol to obtain the relative density of the samples [11]. A rolled wrought Al7075 alloy served as a reference and a Mettler Toledo AE200 weighing system was used following ASTM-B311 standard. On the most promising samples, the optical aperture of a DuraScan G5 indentor (EmcoTest, Austria) was used to perform large micrographs of three different cross-sections per sample along the building direction (thus 150 mm^2 is analysed for each sample). The amount of large pores present in the microstructure was computed by image analysis using ImageJ software. Microfocus X-ray computed tomography (micro-CT)-based morphological characterisation of two samples was performed using an EasyTom XL system (RX Solutions, France). A tungsten target and a LaB6 filament were used. The tube was set in middle focal spot and the applied voltage and current were 100 kV and 48 μA, respectively. After scanning, the radiographs were reconstructed using X-Act reconstruction software (RX Solutions, France). The resulting images had an isotropic voxel size of 1.2 μm. Since the spatial resolution corresponds to three times the voxel size, the minimum size of the observable features is 3.6 μm. Avizo software (ThermoFisher, Bordeaux, France) was used for analysis and 2D/3D visualisation of the sample volume (850 μm × 1050 μm × 1300 μm) and internal structure.

A Keyence VHX-7000 optical microscope was used to image etched samples (1 min with Keller reagent). The melt pool dimensions were obtained by averaging at least six melt pools from the last layer (to be able to observe the full melt pool).

Table 1
ICP-OES measurement performed on the Al7075 and ZrH_2 mix powder feedstock as well as on three L-PBF samples processed with two different scanning strategies: one using the single scanning strategy (SS) and two using the pre-sintering strategy (PS)(see Section 3.1). Here are the parameters used to process these samples: SS processed using P = 164 W, v = 200 mm/s and HS = 100 μm, PS opti using P = 164 W, v = 400 mm/s and HS = 50 μm and PS un-opti using P = 164 W, v = 200 mm/s and HS = 100 μm. The loss of Mg and Zn for these three samples is evaluated based on the specific composition used to process them (see Table A.3).

	Scan. strat.	[%wt]	Al	Cr	Cu	Fe	Mg	Si	Zn	Zr	Mg loss [%]	Zn loss [%]
Powder mix	/	*Mean*	bal	0.2	1.53	0.08	2.39	0.03	5.49	1.79	/	/
	/	*St. Dev.*	–	0.00	0.06	0.01	0.03	0.01	0.21	0.08	/	/
L-PBF sample	SS (opti)	*Mean*	bal	0.22	1.60	0.08	1.82	0.03	3.55	1.75	25	39
	PS (opti)	*Mean*	bal	0.22	1.60	0.08	1.76	0.03	3.32	1.82	27	37
	PS (un-opti)	*Mean*	bal	0.22	1.58	0.08	1.65	/	2.98	1.89	31	47

Electron backscattered diffraction (EBSD) analyses were performed using a Helios NanoLab 600i FEG-SEM equipped with a HKL EBSD detector and an Aztec acquisition software. The Channel 5.0 software was used to analyse the EBSD data. An acceleration tension of 25 keV and a current of 5.5 nA were used for the measurements. For the low and the high magnification maps step sizes of 0.5 μm and 0.1 μm were respectively used. These two types of maps allow to analyse the large columnar grains as well as the melt pools morphology and the fine equiaxed grains respectively. Given the irregular nature of the investigated microstructures, the grains were classified into three populations: fine equiaxed, medium equiaxed and columnar. Small equiaxed grains are defined as being smaller than 2 μm. The medium size grains are larger than 2 μm and are not columnar. Columnar grains are defined as grains with an equivalent diameter larger than 3 μm and an aspect ratio larger than 2 [47]. To obtain the mean size of each grain population with enough statistics, the high resolution maps were used to measure fine grains while low resolution maps were used to measure medium and columnar grains. Due to this highly heterogeneous microstructure, it was chosen to avoid using the mean grain size. The large number of really small grains decrease artificially this average grain size, since each grain has the same weight. Instead, it was chosen to use a surface weighted average to represent better the real microstructure of the sample. For each category of grains (fine, medium and columnar), its mean size was weighted according to the surface fraction occupied by this category (extracted from the large EBSD maps). A schematic summary of the EBSD computations methodology is available in Figure A.2. Samples for microstructural characterisation were mechanically polished using diamond sprays with a minimum particle size of 1 μm and finally with 0.04 μm colloidal silica suspension.

3. Results and discussion

3.1. Towards high density L-PBF Zr-modified Al7075

Fig. 1 illustrates the density of Al7075 samples processed using the parameter sets included in Table A.1 as a function of the volumetric energy density (VED)($\frac{P}{v \times HS \times t}$) [8]. In all cases, the density is lower than 98%. The samples with the highest densities were analysed using OM and all exhibit severe cracking (an example of the defect distribution of one of those specimens is shown in the inset of Fig. 1 and additional micrographs for a wide range of VED are shown in supplementary Figure A.3). The origin of cracks can be unambiguously attributed to hot cracking since they are intergranular and parallel to the building direction as extensively reported in literature for L-PBF 7xxx alloys [16–19]. It was also formally verified by analysing the fracture surface of a L-PBF un-modified Al7075 manually broken (see supplementary Figure A.4 clearly exhibiting hot cracks fracture surface). The inset of Fig. 1 also contains an EBSD map of the same sample illustrating that the processed samples have the characteristic columnar microstructure. The average grain length and width of that sample are 27 ± 31 and 8 ± 4 μm respectively. Hot cracking happens at the end of solidification and takes place preferentially along grain boundaries as shown by the EBSD mapping (see inset Fig. 1) [15,21]. To avoid hot cracking, ZrH_2 was added to the Al7075 pre-alloyed powder as Zr is a well known efficient grain refiner generating a fine equiaxed microstructure [22–33]. An amount of approximatively 2wt% of ZrH_2 was selected to allow enough grain refinement while maximising mechanical properties as previously shown in Nie et al. study on L-PBF Al-4.24Cu-1.97Mg-0.56Mn [26]. ICP analyses performed on this powder mix reveal an average value of 1.8wt%Zr (see Table 1). The following analyses will be performed only on this Al7075+1.8%Zr alloy.

Fig. 2(a) compares the variation of the density of Al7075+1.8%Zr parts manufactured using SS (red dots) and a PS (green dots) strategies as a function of the VED (see complete list of samples in supplementary Table A.2). Please note that the use of VED to quantify the energy density for the PS strategy is inherently flawed. Indeed, for this strategy, each layer is scanned twice which complicates the computation of energy density transferred to the sample. Nevertheless, it was chosen to use the VED of the second high power scan of the PS strategy to allow a direct comparison with the SS on a single graph. To the author's knowledge, no dedicated rule to compute the energy for a PS strategy (or double scanning in general) is proposed in literature. The use of the single scanning (SS) strategy leads to relative densities at best around 98% (with the highest density reached being 98.2% using P = 60 W, v = 200 mm/s and HS = 100 μm leading to a 273 J/mm^3 VED, see Table A.2). The PS strategy allows to systematically improve this relative density as highlighted in green on Fig. 2. A maximum relative density of 99.4% (using P = 60 W, v = 400 mm/s and HS = 50 μm leading to a 273 J/mm^3 VED, see Table A.2) can be reached using this unconventional scanning strategy.

The addition of Zr led to the disappearance of hot cracking (see more details in Section 3.2). The inset of Fig. 2 illustrates, as an example, an optical microscopy image of one sample with high density, which was manufactured using the PS strategy. Moreover, these micrographs allow to analyse the pores larger than 50 μm which are detrimental for fatigue performances [9]. Fatigue will not be analysed in this paper but it is a mechanical property that is certainly pertinent for aerospace applications of these high strength alloys. Moreover, it is already shown in literature that large pores (especially lack of fusion pores) initiate fatigue failure for Scalmalloy® produced by L-PBF (a reference alloy for high strength Al L-PBF alloys) [48,49].

Fig. 2(b) shows the count of only the large pores for five different samples whose processing parameters are referenced based on optical microscopy image analysis. The four samples processed using the PS strategy exhibiting the highest density based on Archimedes analysis were selected. Additionally, the sample processed using the SS strategy exhibiting the highest density was also selected to compare the amount of large pores generated by both scanning strategies. PS strategy results in a global decrease of large pores compared to the SS strategy. The optimised set of parameters selected is P = 164 W, v = 400 mm/s

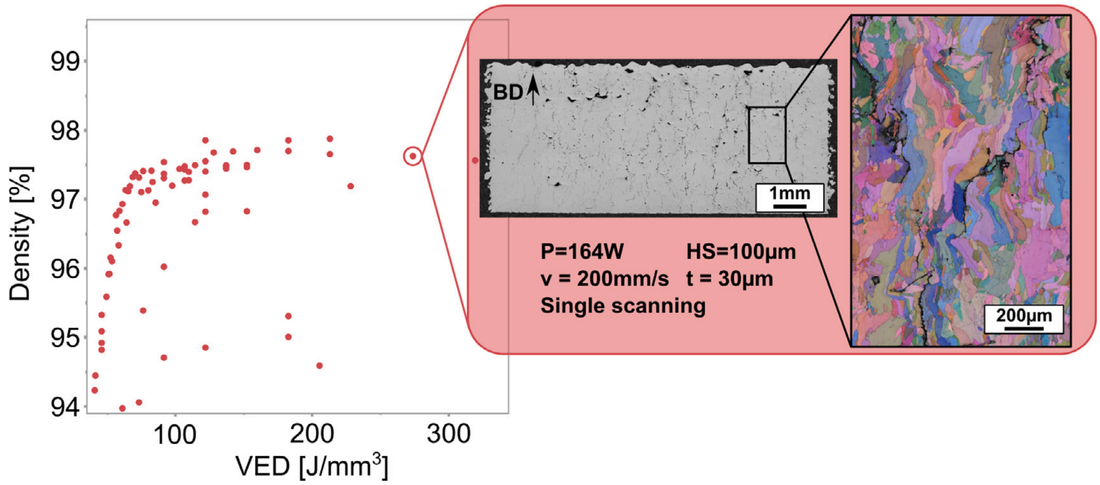

Fig. 1. Relative density of Al7075 parallelepipeds obtained by Archimedes method as a function of the volumetric energy density (VED). The samples were processed using single scanning classical strategy. A cross-section of the sample built using the same parameters as selected in red in Fig. 2(b) is highlighting hot cracking. A low magnification large Euler angle EBSD map of the same sample is also displayed. (For interpretation of the references to colour in this figure legend, the reader is referred to the web version of this article.)

and HS = 50 μm using the PS scanning strategy. This set is selected because it generates the lowest amount of pores larger than 50 μm while avoiding pores larger than 100 μm. Aiming at understanding the effect of PS scanning strategy, it will be compared with a sample processed using the parameters leading to the highest density using SS strategy: P = 164 W, v = 200 mm/s and HS = 100 μm. These two set of parameters share the same VED of 273 J/mm^3. The micrographs used to obtain the large pores statistics for these two sets of parameters are shown in supplementary Figure A.5. To assess the reproducibility of the Archimedes results obtained for both samples processed using the selected SS and PS sets of parameters, 11 SS strategy samples and 7 PS strategy samples were produced distributed on several building jobs. The SS samples exhibit a mean Archimedes relative density of 97.8% $\pm$ 0.4 while the PS samples a density of 99.1% $\pm$ 0.2. The double of standard deviation of the SS relative density highlights the higher reproducibility of the samples produced using the PS strategy.

Micro-CT was performed on the two samples identified here-above (highlighted in Fig. 2(b) by a red and a green boxes): one single scanned sample and the optimised pre-sintered sample. Fig. 3 shows that the volume fraction of pores is more than ten times smaller for the pre-sintered sample than for the single-scanned one. Fig. 3 confirms what was already concluded from the Archimedes method and from the examination of the defect structure imaged using OM. According to the micro-CT scan, a relative density of 99.91% is reached when the optimised processing conditions (for PS scanning strategy) are used. The relative density obtained by micro-CT is preferred to the one obtained by the Archimedes method (see Fig. 2(a)) and will serve as comparison to the values referenced in literature. Indeed, Archimedes method is efficient and useful for the large comparison performed in this work but it is difficult to compare with literature. The choice of a reference value to compute the relative density impacts greatly the final value and differs between authors [41] or is not mentioned [31,36,39]. Thus, some studies select the micro-CT results as the definitive relative density value [35,42]. Regarding pores morphology, no large irregular pores (lack-of-fusion pores) are observed for the pre-sintered specimen. This is confirmed by the pores size distribution shown on Fig. 3(c). The distribution is similar for both strategies with around 90% of pores having a diameter below 20 μm. However, no pores exhibit a diameter larger than 60 μm for the PS scanning strategy compared to 0.28% (10 pores for a volume of 850 μm × 1050 μm × 1300 μm) for the SS scanning strategy. This difference is also reflected by the mean volumetric size of the pores: 122 μm for SS strategy compared to 35 μm for PS strategy. These pores larger than 60 μm are characterised by a very low sphericity (see Fig. 3(d)), clearly identifying them as lack of fusion pores. Moreover, the PS sample also contains around 4 times less pores smaller than 20 μm than the SS sample (578 pores for the PS sample and 2362 pores for the SS sample). It can be quantitatively compared since the volume analysed for the two specimen is identical (850 μm × 1050 μm × 1300 μm). The high differences in relative density and in pores morphology observed between the SS and PS strategy as well as the effect of the PS strategy on the microstructure will be explained in Section 3.2.

It is important to note that the choice of a PS sample processed using P = 164 W, v = 400 mm/s, HS = 50 μm to compare to a single scan sample processed using P = 164 W, v = 200 mm/s, HS = 100 μm is not straightforward. Indeed, the influence of the change in the parameters could influence the comparison, even if these two sets of parameters are the optimised for PS and SS strategy respectively. Thus, a tomography scan on a PS sample processed using the same parameters than the SS sample of Fig. 3(a) was performed as shown in supplementary Figure A.7. The same total volume (but with a different aspect ratio, larger length and smaller width) as samples of Fig. 3 was analysed and a relative density of 99.7% was obtained. Some Lack of fusion pores also remain present in this PS un-optimised sample, attesting a lack of overlapping between layers or adjacent scanning tracks. Thus it is more interesting to compare the optimised PS strategy since it allows to avoid these lack of pores. Figure A.7 also proves that, at constant parameters, PS strategy still improves significantly the relative density (+0.89%).

3.2. Understanding the effect of pre-sintering on the microstructure

To understand the effect of PS scanning strategy on the porosity level of Al7075+1.8%Zr, its impact on the melt pool morphology must be analysed beforehand. Fig. 4 shows the mesostructure of a single scanned and a pre-sintered sample. In particular, the last layer is highlighted in the insets of Fig. 4 to allow measuring the melt pool size. The Keller etching reveals the grain boundaries and allows to distinguish the melt pool borders. Moreover, Fig. 4(c) shows a pre-sintered sample where the last layer is only processed using the first half-power scan of the PS strategy. This highlights the effect of the first scan on the mesostructure. The use of the SS strategy gives rise to large melt pools of 97 μm depth and 231 μm width (see Fig. 4(a)). In turn, the first low-power pass of the PS strategy results in shallower melt pools, with an average depth of 47 μm and average width of 98 μm (see Fig. 4(c)). Afterwards, the second scan generates larger melt pool of

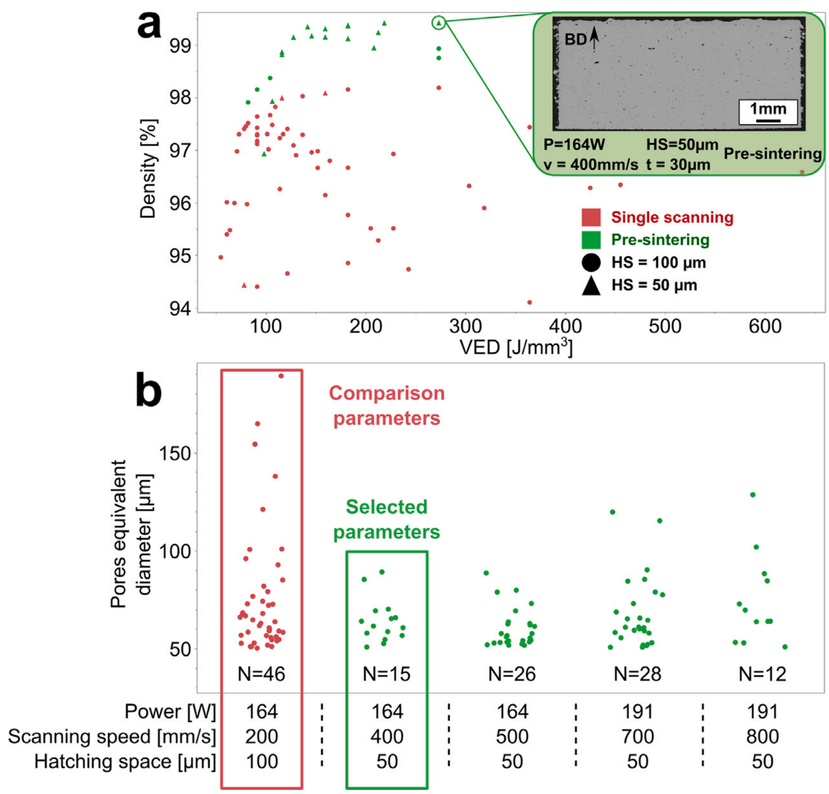

Fig. 2. (a) Relative density of Al7075+1.8%Zr parallelepipeds obtained by Archimedes method as a function of the volumetric energy density (VED). In red, the samples were processed using the single scan classical strategy and in green using the pre-sintering strategy. An optical microscopy cross-section of the sample built using the optimised parameters is also displayed. (b) Equivalent diameters of pores larger than 50 μm obtained by image analysis of optical micrographs. The number of pores (N) is indicated below each scatter plot as well as the parameters used to build the samples. (For interpretation of the references to colour in this figure legend, the reader is referred to the web version of this article.)

74 μm depth and 140 μm width (see Fig. 4(b)). Thus, the final melt pool is thinner and shallower than the single scanned melt pools.

Earlier works have reported the formation of shallower melt pools when using a double scan strategy, in which both passes are made with the same process parameters. Griffith et al. [50], have observed that, while processing an Al-Mg-Zr (Addalloy™) by L-PBF using a double scanning strategy, a double melt pool structure could be observed. Their second scanning pass generated shallower melt pools due the poorer interaction between the laser and bulk aluminium compared to the laser-powder interaction. Gusarov et al. [51] have modelled the laser-powder interaction and showed that due to multiple reflections of the laser inside a powder bed, metallic powder exhibit a higher absorptivity compared to flat metallic surfaces. Boley et al. [52] combined modelling and experimental measurements to prove that Al powder absorptivity is more than two times larger than for a flat-Al surface. In the PS strategy of the present work, which has been scarcely utilised to date, unlike for double scanning strategy, Fig. 4 showed that the melt pools generated by the first low power scan are smaller than for the second full power scan. Despite the higher absorptivity of the powder, the pre-scanning power of 82 W is still quite low. Therefore, the second higher power scan (164 W) combined with the higher reflectivity of the solid surface (resulting from the first scan) generate melt pools larger than for the first scan but smaller than for a SS strategy.

Fig. 5 compares the microstructure of samples processed using the SS and the PS strategies. For each sample, EBSD maps in the BD corresponding to high and low magnifications are shown on Fig. 5(a,b). For both scanning strategies, a bi-modal grain structure is formed which is characteristic of the grain-refined L-PBF aluminium alloys. This bi-modal microstructure is composed of fine equiaxed grains at the bottom of the MP and of columnar grains at the heart of the melt pool (MP). This heterogeneity can be explained by a difference of cooling rate between these two zones during solidification. The slower cooling rate at the bottom of the MP allows the formation of Al_3Zr $L1_2$ precipitates acting as preferential nucleation sites for fine equiaxed grains [40,47]. At the heart of the MP, closer to the laser heat source, Zr does not have enough time to form grain refining precipitates and remains trapped in solid solution due to the faster cooling rate [40,47]. These grain refining precipitates were formally identified in supplementary Figure A.6 but will not be analysed in details in this work.

The surface weighted average grain size for the PS strategy (1.4 μm) is smaller compared to SS strategy (1.8 μm) (see Fig. 5(c)). This difference is generated by the slightly smaller fine, medium and columnar grains combined with the smaller area fraction occupied by medium and columnar grains for the PS strategy. Moreover, Fig. 5(d) illustrates a small shift of the grain size distribution towards smaller values. The grain size distribution was truncated to highlight the effect of scanning strategy on fine grains. The complete size distribution is shown in supplementary Figure A.8. Indeed, the sample processed using the PS strategy exhibits a higher number fraction (79%) of grains below 1 μm compared to the one processed using SS strategy (58%). The general grain refinement in the case of PS strategy can be explained by two phenomena exploiting literature.

Firstly, Griffith et al. [50], as mentioned before, observed the formation of a double melt pool morphology generated by the rescanning of a previously scanned layer. As a result, they observed a decrease of the grain size when a double scanning strategy is used. For the case of this study, this effect is of secondary importance since the melt pool generated by the second scan is deeper than the MP generated by the first low power scan. Secondly, Ekubaru et al. [53] analysed the effect of the hatching space on the grain structure of L-PBF processed Scalmalloy®. They measured an increase from 35% to 60% of the volume fraction of ultrafine grains (below 2 μm) when the hatching space

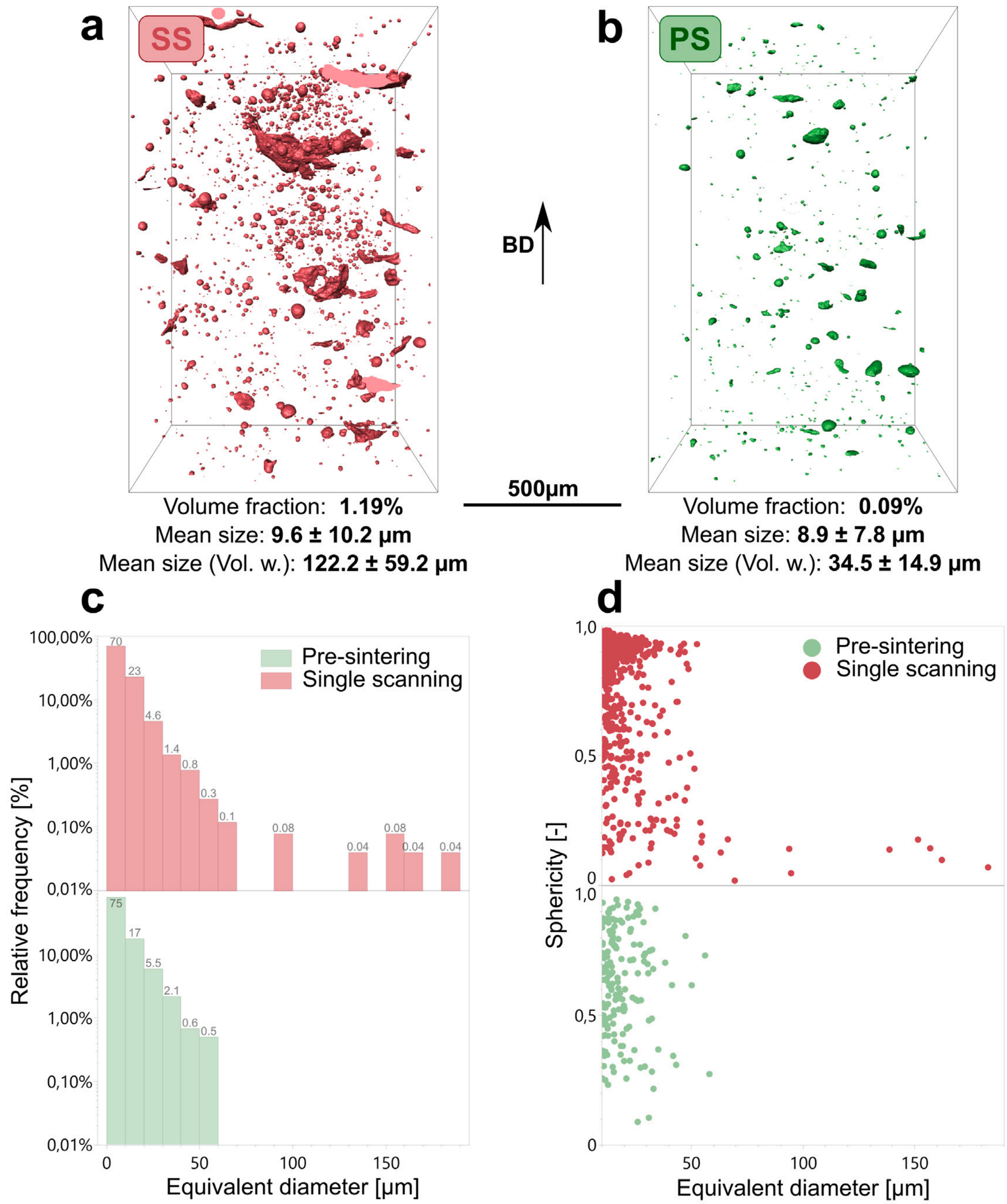

Fig. 3. Comparison of the porosity for two different building conditions: (a) sample processed with single scanning strategy (P = 164 W, v = 200 mm/s, HS = 100 µm) and (b) with the pre-sintering strategy (P = 164 W, v = 400 mm/s, HS = 50 µm). These results were obtained by micro-CT with a voxel size of 1.2 µm. The VED is kept unchanged but the exact parameters are selected for optimal density (see Fig. 2). (c) Pores size distribution for both conditions. (d) Comparison of pores sphericity and diameter.

is decreased from 100 µm to 60 µm. This decrease of hatching space corresponds to an increase of the overlapping between two adjacent scanning tracks. To summarise, Ekubaru et al. [53] demonstrated that a smaller hatching space increase the surface fraction of fine grains due to a higher overlapping between melt pools. In this study, the analysis is less straightforward since the hatching space is changed from 100 µm to 50 µm but the speed is also increased from 200 mm/s to 400 mm/s and the scanning strategy is different. In order to apply the conclusion of Ekubaru et al. [53] to our work, the overlapping between two adjacent melt pools must be evaluated. Using the melt pool size obtained from Fig. 4, a 57% overlap is reached for SS strategy and a 64% overlap is reached for PS strategy. In conclusion, this increase in the overlapping combined with the use of two scans per layer may explain the grain refinement observed when using the PS scanning strategy.

The effect of the PS scanning strategy on the microstructure being explained, its improvement of the relative density observed on Fig. 3 should be understood. To explain the effect of this scanning strategy and more generally the effect of the double scanning, a few hypotheses can be extracted from literature. Firstly, it can be hypothesised that the first low power scan dries the powder limiting the formation of hydrogen pores [46]. However, for this study, the first scan already melts the powder and thus, it does not really act as drying step for the powder.

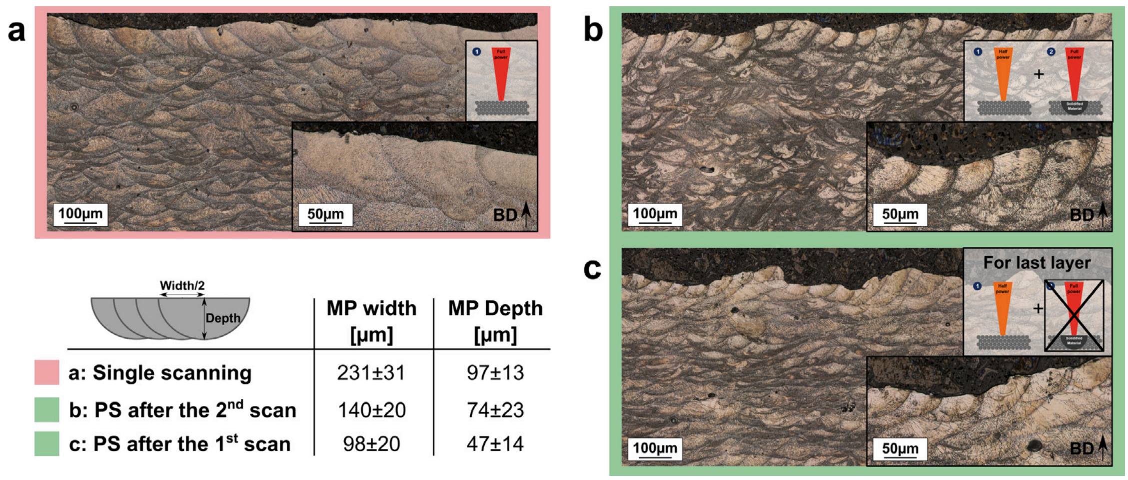

	MP width [µm]	MP Depth [µm]
a: Single scanning	231±31	97±13
b: PS after the 2nd scan	140±20	74±23
c: PS after the 1st scan	98±20	47±14

Fig. 4. Optical micrographs of etched samples. (a) Sample produced using the single scanning strategy and (b) using the pre-sintering strategy. Sample (c) was produced using the same parameters as (b) except for the last layer where only the first scan (half-power scan) of the pre-sintering strategy was performed. The melt pool size measurements performed on the last layer of each samples are provided in the accompanying table.

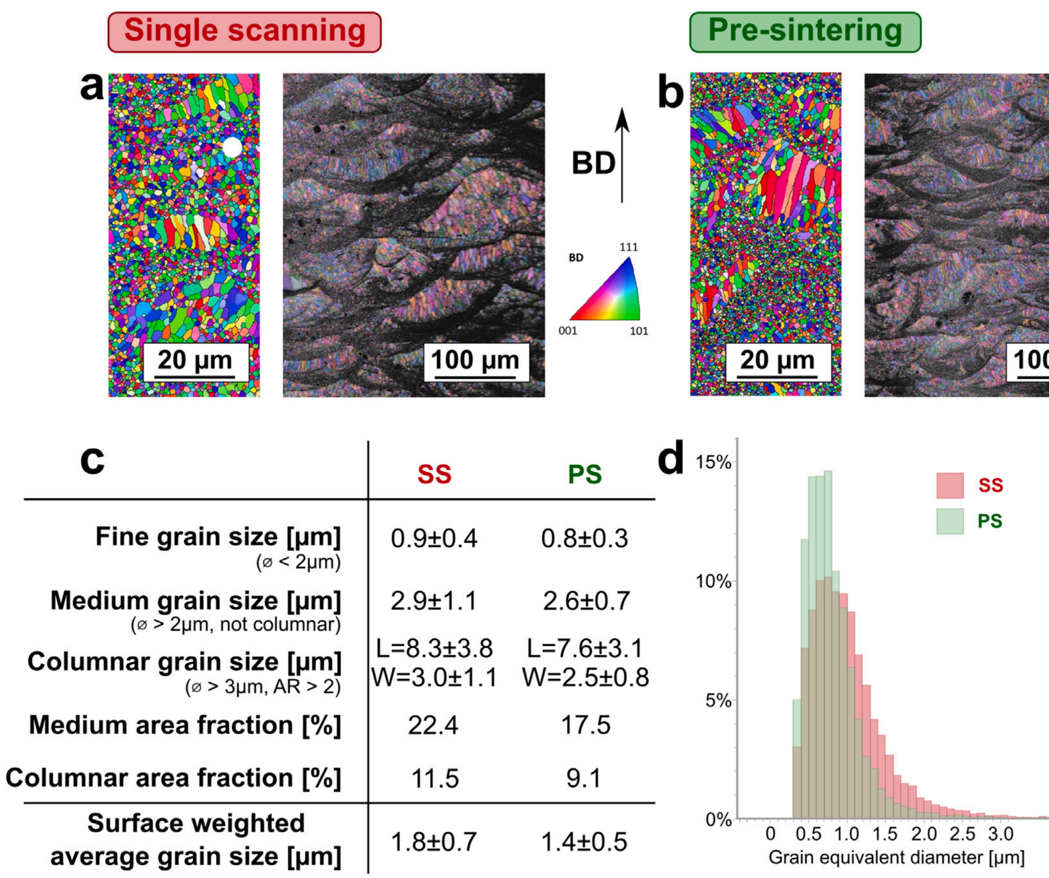

c	SS	PS
Fine grain size [µm] (⌀ < 2µm)	0.9±0.4	0.8±0.3
Medium grain size [µm] (⌀ > 2µm, not columnar)	2.9±1.1	2.6±0.7
Columnar grain size [µm] (⌀ > 3µm, AR > 2)	L=8.3±3.8 W=3.0±1.1	L=7.6±3.1 W=2.5±0.8
Medium area fraction [%]	22.4	17.5
Columnar area fraction [%]	11.5	9.1
Surface weighted average grain size [µm]	1.8±0.7	1.4±0.5

Fig. 5. (a) Detailed high magnification IPF in the building direction EBSD map and a low magnification large Euler angle EBSD map of as-built Al7075+1.8%Zr processed using single scanning strategy (P = 164 W, v = 200 mm/s and HS = 100 µm, see Fig. 2(b)). (b) Same EBSD analyses for a sample processed using the pre-sintering strategy (P = 164 W, v = 400 mm/s and HS = 50 µm, see Fig. 2(b)). (c) Grains statistics based on the EBSD mapping of these two conditions. (d) Comparison of the grain size distribution for single scanning strategy in red and pre-sintering strategy in green based on the detailed EBSD maps. (For interpretation of the references to colour in this figure legend, the reader is referred to the web version of this article.)

Another hypothesis that is discussed in literature is the outgassing hypothesis. Before entering into details, the principle of this phenomenon is that a second scan can allow the gas pores to exit the melt pool during processing and so improves density. For the majority of materials processed by L-PBF, these gas pores are generated by hydrogen coming from powder moisture, are pre-existing in the powder or come from Argon trapped in the melt pool during processing. In this study, in addition to hydrogen and argon pores, gas pores can be generated by the preferential evaporation of Zn and Mg during processing [8,30,38]. To assess quantitatively the degree of evaporation, the composition of the L-PBF processed samples was also analysed. ICP-OES was performed on the two samples analysed by micro-CT in Fig. 3, which were processed using the SS and PS strategies (see Table 1). Comparing these values after processing with the composition of the powder reveals a loss of Mg and Zn. Losses are computed based on the composition of the specific powder batches used for each building job (see supplementary Table A.3 for the ICP of the specific powders) and not based on the global composition of Table 1. For the SS strategy, a loss of 25 and 39% of Mg and Zn respectively is observed. A similar loss of 27% Mg and 37% Zn is evidenced by the analyses for the PS strategy. The resulting Mg and Zn wt% after L-PBF are thus below the standards required for Al7075 (between 2.1 and 2.9% for Mg and between 5.1 and 6.1% for Zn [54]). These losses due to evaporation are non-negligible and must be taken into consideration for the understanding of the effect of PS scanning strategy on the porosity. For the current discussion, the Mg and Zn losses are not significantly different for the two strategies and thus cannot explain the density difference.

To assess the individual effect of the PS scanning strategy on Zn and Mg evaporation, an additional ICP analysis was performed on the PS sample analysed in supplementary Figure A.7 processed using the same parameters as the optimised SS sample (P = 164 W, v = 200 mm/s, HS = 100 μm, see ICP result in Table 1). A Mg and Zn loss of 31% and 47% respectively was obtained. Thus, at constant parameters, the evaporation of Mg and Zn is favoured by the PS strategy. However, this loss is decreased while the density is improved when the PS strategy process parameters are optimised as shown by the ICP result (see Table 1). It will also facilitate the discussion to have a similar amount of Zn and Mg evaporation for the SS and PS optimised samples.

In what concerns the outgassing hypothesis, Weingarten et al. state that the use of a low scanning speed improves the ability to outgas the hydrogen trapped in the melt pool that results in gas pores after solidification [46]. By using a low scanning speed, it decreases the cooling rate and therefore increases the time during which the melt pool is in liquid state [55]. More time is therefore available for gases to escape the melt pool and avoid being trapped in the final part. It can also explain the high densities (larger than 99.5%) obtained for L-PBF Al7075 in two different studies in which a scanning speed of 160 mm/s [35] and 50 mm/s [44] were respectively used. Back to the present study, for the optimised PS strategy parameters, the scanning speed is higher (400 mm/s) but the melt pools have a lower depth facilitating outgassing. Xie et al. [45] demonstrated that a second laser scanning that generates a deeper melt pool than the first one can remove defect (keyhole or lack of fusion) since it remelts the whole melt pool that was formed beforehand. Lv et al. [55] observed the same effect of laser remelting on various defect for L-PBF Ti-6Al-4V. Finally, de Formanoir et al. [56] showed by operando observation by X-ray imaging of the L-PBF process of 316L stainless steel the healing of keyhole pores by laser remelting. They directly observed that laser remelting triggers outgassing of keyhole pores and that an increase of the time of interaction between the laser and the defects (thus an increase of the time the melt pool is in liquid state) improves the healing efficiency. For this study, Fig. 4(b) clearly highlights the deeper MP generated by the second scan compared to the MP generated by the first scan shown on Fig. 4(c). Thus, it matches the condition stated by Xie et al. for the second scan to remove defects remaining after a first scan. Moreover, Fig. 3 clearly shows that no lack of fusion pores are observed when using a PS strategy.

In the following, identification of the type of gas pores (originated by hydrogen trapping, argon trapping or by Zn/Mg evaporation) is carried out. Table 2 shows the amount of hydrogen in powders and in L-PBF samples obtained using an ONH analyser, giving access to hydrogen content of the whole L-PBF samples (solid + pores). The initial pre-alloyed Al7075 powder and the two L-PBF samples (SS and PS) all contain approximately 0.005% of hydrogen. Therefore, the scanning strategy has no effect on the final amount of hydrogen in the L-PBF samples. Moreover, since the Al7075+1.8%Zr powder contains a significantly higher amount of hydrogen (roughly a factor 10), the hydrogen present in the powder obviously comes from the addition of ZrH_2. However, the final L-PBF parts do not contain additional hydrogen compared to the 7075 powder. Therefore, the addition of ZrH_2 to the Al7075 pre-alloyed powder does not generate hydrogen pores in the L-PBF samples. Furthermore, lack of influence of the scanning strategy on the amount of hydrogen of the two solid samples analysed shows that the PS scanning strategy does not outgas more hydrogen pores compared to SS scanning strategy.

Table 2
Amount of hydrogen in the Al7075 pre-alloyed powder and the Al7075+ZrH_2 powder mix powder feedstock as well as on two L-PBF samples processed with two different scanning strategies using the optimised process parameters (highlighted in Fig. 2(b)): the single scanning strategy (SS) and the pre-sintering strategy (PS).

	Type of powder	Amount of H [%wt]
Powder	*Al7075*	0.005 ± 0.003
	Al7075+1.8%Zr	0.048 ± 0.002
	Scan.strat.	Amount of H [%wt]
L-PBF sample	*SS*	0.005 ± 0.008
	PS	0.005 ± 0.002

Gathering these various results and literature survey, two main points can be concluded on the effect of PS strategy. Firstly, the use of higher VED is possible for the PS strategy without forming keyhole porosity as it is the case for the SS strategy (see bottom right corner of Fig. 2(a)). The use of PS with parameters generating a high VED allows to obtain a large enough overlapping between the layers and adjacent scan tracks avoiding large lack of fusion pores. Secondly, PS greatly decreases the amount of small gas pores remaining in the final microstructure. The ONH analysis shown that it cannot be due to hydrogen pores since the final amount of H in both SS and PS optimised samples is the same (see Table 2). Thus the better PS density could be due to an easier outgassing of Ar pores due to the smaller melt pool generated by the PS strategy. In addition, this higher density could also result from a remelting of small Zn and Mg pores by the second scan of the PS strategy. Indeed, this PS strategy is remelting the entire first melt pool generated by the low power scan. This all results in an optimised PS strategy that generates an outstanding 99.9% relative density.

4. Conclusion

This study demonstrated that using a pre-sintering scanning strategy, composed of a low laser power first scan followed by a higher power second scan allows to process Al7075+1.8%Zr samples that can reach a CT-scan density of 99.9% without experiencing hot cracking. This pre-sintering (PS) strategy generates shallower melt pools exhibiting a bi-modal grain microstructure composed mainly of small equiaxed grains.

It was shown that the hydrogen desorption is not a major factor dictating the density for L-PBF Al7075+1.8%Zr. Instead, PS strategy avoid lack of fusion pores and remelts remaining defects left by the first low power scan using a larger melt pool generated by the second scan. Outgasing of small Ar pores could also play a role on the improvement of density of the PS strategy.

This rarely used scanning strategy could be applied to other material generating a lot of evaporation during the L-PBF process and help improve their processability. This would help broaden the material palette available for L-PBF and so increase the number of potential applications for L-PBF.

CRediT authorship contribution statement

Nicolas Nothomb: Writing – original draft, Visualization, Project administration, Methodology, Investigation, Funding acquisition, Formal analysis, Conceptualization. **Ignacio Rodriguez-Barber:** Methodology, Investigation, Conceptualization. **María Teresa Pérez-Prado:** Writing – review & editing, Supervision, Resources, Conceptualization. **Norberto Jimenez Mena:** Writing – review & editing, Resources, Conceptualization. **Grzegorz Pyka:** Writing – review & editing, Investigation, Conceptualization. **Aude Simar:** Writing – review & editing, Supervision, Resources, Methodology, Funding acquisition, Conceptualization.

Declaration of competing interest

The authors declare that they have no known competing financial interests or personal relationships that could have appeared to influence the work reported in this paper.

Acknowledgements

Nicolas Nothomb is a FRIA grantee of the Fonds de la Recherche Scientifique de Belgique - FNRS, Belgium and gratefully acknowledges their support. Marie-Noëlle Avettand-Fénoël and Maya Marinova are acknowledged for their help with the supplementary TEM experiments.

Appendix A. Supplementary data

Supplementary material related to this article can be found online at https://doi.org/10.1016/j.addlet.2024.100253.

Data availability

Data will be made available on request.

References

[1] T. DebRoy, et al., Scientific, technological and economic issues in metal printing and their solutions, Nature Mater. (ISSN: 14764660) 18 (10) (2019) 1026–1032, http://dx.doi.org/10.1038/s41563-019-0408-2, URL http://dx.doi.org/10.1038/s41563-019-0408-2.

[2] T. DebRoy, et al., Additive manufacturing of metallic components – Process, structure and properties, Prog. Mater. Sci. (ISSN: 00796425) 92 (2018) 112–224, http://dx.doi.org/10.1016/j.pmatsci.2017.10.001.

[3] Paul A. Rometsch, et al., Review of high-strength aluminium alloys for additive manufacturing by laser powder bed fusion, Mater. Des. (ISSN: 0264-1275) 219 (2022) 110779, http://dx.doi.org/10.1016/j.matdes.2022.110779, URL https://doi.org/10.1016/j.matdes.2022.110779.

[4] A.T. Clare, et al., Alloy design and adaptation for additive manufacture, J. Mater. Process. Technol. (ISSN: 09240136) 299 (September 2021) (2022) http://dx.doi.org/10.1016/j.jmatprotec.2021.117358.

[5] Dirk Herzog, et al., Additive manufacturing of metals, Acta Mater. (ISSN: 13596454) 117 (2016) 371–392, http://dx.doi.org/10.1016/j.actamat.2016.07.019, URL http://dx.doi.org/10.1016/j.actamat.2016.07.019.

[6] Rajiv S. Mishra, Saket Thapliyal, Design approaches for printability-performance synergy in Al alloys for laser-powder bed additive manufacturing, Mater. Des. (ISSN: 18734197) 204 (2021) 109640, http://dx.doi.org/10.1016/j.matdes.2021.109640, URL https://doi.org/10.1016/j.matdes.2021.109640.

[7] Nesma T. Aboulkhair, et al., Reducing porosity in AlSi10Mg parts processed by selective laser melting, Addit. Manuf. (ISSN: 22148604) 1 (2014) 77–86, http://dx.doi.org/10.1016/j.addma.2014.08.001, URL http://dx.doi.org/10.1016/j.addma.2014.08.001.

[8] Nesma T. Aboulkhair, et al., 3D printing of aluminium alloys: Additive manufacturing of aluminium alloys using selective laser melting, Prog. Mater. Sci. (ISSN: 00796425) 106 (July) (2019) 100578, http://dx.doi.org/10.1016/j.pmatsci.2019.100578, URL https://doi.org/10.1016/j.pmatsci.2019.100578.

[9] Juan Guillermo Santos Macías, et al., Fatigue crack nucleation and growth in laser powder bed fusion AlSi10Mg under as built and post-treated conditions, Mater. Des. (ISSN: 02641275) 210 (210) (2021) http://dx.doi.org/10.1016/j.matdes.2021.110084, URL https://linkinghub.elsevier.com/retrieve/pii/S0264127521006390.

[10] O Poncelet, et al., Critical assessment of the impact of process parameters on vertical roughness and hardness of thin walls of AlSi10Mg processed by laser powder bed fusion, Addit. Manuf. (ISSN: 2214-8604) 38 (July 2020) (2021) 101801, http://dx.doi.org/10.1016/j.addma.2020.101801, URL https://doi.org/10.1016/j.addma.2020.101801.

[11] Julie Gheysen, et al., Efficient optimization methodology for laser powder bed fusion parameters to manufacture dense and mechanically sound parts validated on AlSi12 alloy, Mater. Des. (ISSN: 02641275) 199 (2020) 109433, http://dx.doi.org/10.1016/j.matdes.2020.109433, URL https://doi.org/10.1016/j.matdes.2020.109433.

[12] Shafaqat Siddique, Muhammad Imran, Frank Walther, Very high cycle fatigue and fatigue crack propagation behavior of selective laser melted AlSi12 alloy, Int. J. Fatigue 94 (2017) 246–254.

[13] Lv Zhao, et al., Review on the correlation between microstructure and mechanical performance for laser powder bed fusion AlSi10Mg, Addit. Manuf. (ISSN: 22148604) 56 (May) (2022) 102914, http://dx.doi.org/10.1016/j.addma.2022.102914, URL https://doi.org/10.1016/j.addma.2022.102914.

[14] Yue Li, et al., Recent advances in hot tearing during casting of aluminium alloys, Prog. Mater. Sci. (ISSN: 00796425) 117 (September 2020) (2021) 100741, http://dx.doi.org/10.1016/j.pmatsci.2020.100741, URL https://doi.org/10.1016/j.pmatsci.2020.100741.

[15] Sindo Kou, A criterion for cracking during solidification, Acta Mater. (ISSN: 13596454) 88 (2015) 366–374, http://dx.doi.org/10.1016/j.actamat.2015.01.034, URL http://dx.doi.org/10.1016/j.actamat.2015.01.034.

[16] Ting Qi, et al., Selective laser melting of Al7050 powder: Melting mode transition and comparison of the characteristics between the keyhole and conduction mode, Mater. Des. (ISSN: 18734197) 135 (2017) 257–266, http://dx.doi.org/10.1016/j.matdes.2017.09.014, URL https://doi.org/10.1016/j.matdes.2017.09.014.

[17] Wojciech Stopyra, et al., Laser powder bed fusion of AA7075 alloy: Influence of process parameters on porosity and hot cracking, Addit. Manuf. (ISSN: 22148604) 35 (November 2019) (2020) http://dx.doi.org/10.1016/j.addma.2020.101270, URL https://linkinghub.elsevier.com/retrieve/pii/S2214860420306424.

[18] R. Mertens, et al., Application of base plate preheating during selective laser melting, Procedia CIRP (ISSN: 22128271) 74 (2018) 5–11, http://dx.doi.org/10.1016/j.procir.2018.08.002, URL https://doi.org/10.1016/j.procir.2018.08.002.

[19] N. Kaufmann, et al., Influence of process parameters on the quality of aluminium alloy en AW 7075 using selective laser melting (SLM), Physics Procedia (ISSN: 18753892) 83 (2016) 918–926, http://dx.doi.org/10.1016/j.phpro.2016.08.096.

[20] John H. Martin, et al., 3D printing of high-strength aluminium alloys, Nature (ISSN: 14764687) 549 (7672) (2017) 365–369, http://dx.doi.org/10.1038/nature23894.

[21] Sindo Kou, Solidification and liquation cracking issues in welding, Jom (ISSN: 10474838) 55 (6) (2003) 37–42, http://dx.doi.org/10.1007/s11837-003-0137-4.

[22] Maxence Buttard, et al., Multi-scale microstuctural investigation of a new Al-Mn-Ni-Cu-Zr aluminium alloy processed by laser powder bed fusion, Materialia (ISSN: 25891529) 18 (July) (2021) 101160, http://dx.doi.org/10.1016/j.mtla.2021.101160, URL https://doi.org/10.1016/j.mtla.2021.101160.

[23] Maxence Buttard, et al., Ageing response and strengthening mechanisms in a new Al-Mn-Ni-Cu-Zr alloy designed for laser powder bed fusion, Acta Mater. (ISSN: 13596454) 259 (March) (2023) http://dx.doi.org/10.1016/j.actamat.2023.119271.

[24] Joseph R. Croteau, et al., Microstructure and mechanical properties of Al-Mg-Zr alloys processed by selective laser melting, Acta Mater. (ISSN: 13596454) 153 (2018) 35–44, http://dx.doi.org/10.1016/j.actamat.2018.04.053.

[25] Guichuan Li, et al., Exploiting the rapid solidification potential of laser powder bed fusion in high strength and crack-free Al-Cu-Mg-Mn-Zr alloys, Addit. Manuf. (ISSN: 22148604) 47 (June) (2021) 102210, http://dx.doi.org/10.1016/j.addma.2021.102210, URL https://doi.org/10.1016/j.addma.2021.102210.

[26] Xiaojia Nie, et al., Effect of Zr content on formability, microstructure and mechanical properties of selective laser melted Zr modified Al-4.24Cu-1.97Mg-0.56Mn alloys, J. Alloys Compd. (ISSN: 09258388) 764 (2018) 977–986, http://dx.doi.org/10.1016/j.jallcom.2018.06.032, URL https://doi.org/10.1016/j.jallcom.2018.06.032.

[27] Yanfang Wang, et al., Laser powder bed fusion of Zr-modified Al-Cu-Mg alloy: Crack-inhibiting, grain refinement, and mechanical properties, Mater. Sci. Eng. A (ISSN: 09215093) 838 (January) (2022) 142618, http://dx.doi.org/10.1016/j.msea.2022.142618, URL https://doi.org/10.1016/j.msea.2022.142618.

[28] Raya Mertens, et al., Laser powder bed fusion of high strength aluminum, Mater. Des. Process. Commun. 3 (5) (2020) http://dx.doi.org/10.1002/mdp2.161.

[29] Marvin Schuster, et al., Precipitation in a 2xxx series Al-Cu-Mg-Zr alloy fabricated by laser powder bed fusion, Mater. Des. (ISSN: 02641275) 211 (2021) 110131, http://dx.doi.org/10.1016/j.matdes.2021.110131, URL https://doi.org/10.1016/j.matdes.2021.110131.

[30] A. Martin, et al., Influence of the Zr content on the processability of a high strength Al-Zn-Mg-Cu-Zr alloy by laser powder bed fusion, Mater. Charact. (ISSN: 10445803) 183 (2022) http://dx.doi.org/10.1016/j.matchar.2021.111650.

[31] Lanbo Li, et al., Microstructures and tensile properties of a selective laser melted Al-Zn-Mg-Cu (Al7075) alloy by Si and Zr microalloying, Mater. Sci. Eng. A (ISSN: 09215093) 787 (February) (2020) 139492, http://dx.doi.org/10.1016/j.msea.2020.139492, URL https://doi.org/10.1016/j.msea.2020.139492.

[32] Le Zhou, et al., Microstructure and mechanical properties of Zr-modified aluminum alloy 5083 manufactured by laser powder bed fusion, Addit. Manuf. (ISSN: 22148604) 28 (March) (2019) 485–496, http://dx.doi.org/10.1016/j.addma.2019.05.027, URL https://doi.org/10.1016/j.addma.2019.05.027.

[33] Rong Xu, et al., Laser powder bed fusion of Al-Mg-Zr alloy: Microstructure, mechanical properties and dynamic precipitation, Mater. Sci. Eng. A (ISSN: 09215093) 859 (October) (2022) 144181, http://dx.doi.org/10.1016/j.msea.2022.144181, URL https://doi.org/10.1016/j.msea.2022.144181.

[34] Hailiang Zhao, Tarasankar Debroy, Weld metal composition change during conduction mode laser welding of aluminum alloy 5182, Metall. Mater. Trans. B 32B (February) (2001) http://dx.doi.org/10.1007/s11663-001-0018-6.
[35] Zhiguang Zhu, et al., Superior mechanical properties of a selective-laser-melted AlZnMgCuScZr alloy enabled by a tunable hierarchical microstructure and dual-nanoprecipitation, Materials Today (ISSN: 1369-7021) 52 (January-February 2022) (2021) 90–101, http://dx.doi.org/10.1016/j.mattod.2021.11.019, URL https://doi.org/10.1016/j.mattod.2021.11.019.
[36] C. Galera-Rueda, et al., Icosahedral quasicrystal-enhanced nucleation in Al alloys fabricated by selective laser melting, Addit. Manuf. (ISSN: 22148604) 44 (May) (2021) http://dx.doi.org/10.1016/j.addma.2021.102053.
[37] Xiaohui Liu, et al., A combination strategy for additive manufacturing of AA2024 high-strength aluminium alloys fabricated by laser powder bed fusion: Role of hot isostatic pressing, Mater. Sci. Eng. A (ISSN: 09215093) 850 (March) (2022) 143597, http://dx.doi.org/10.1016/j.msea.2022.143597, URL https://doi.org/10.1016/j.msea.2022.143597.
[38] Guichuan Li, et al., Investigation of solidification and precipitation behavior of Si-modified 7075 aluminum alloy fabricated by laser-based powder bed fusion, Metall. Mater. Trans. A 52A (2021) http://dx.doi.org/10.1007/s11661-020-06073-9.
[39] Bin Huang, et al., Selective laser melting of 7075 aluminum alloy inoculated by Al-Ti-B: Grain refinement and superior mechanical properties, Vacuum 200 (111030) (2022).
[40] Sheng Li, et al., Synchrotron characterisation of ultra-fine grain TiB2/Al-Cu composite fabricated by laser powder bed fusion, Acta Metall. Sin. (ISSN: 21941289) 35 (1) (2022) 78–92, http://dx.doi.org/10.1007/s40195-021-01317-y, URL https://doi.org/10.1007/s40195-021-01317-y.
[41] S.Y. Zhou, et al., Selective laser melting additive manufacturing of 7xxx series Al-Zn-Mg-Cu alloy: Cracking elimination by co-incorporation of Si and TiB2, Addit. Manuf. (ISSN: 22148604) 36 (July) (2020) http://dx.doi.org/10.1016/j.addma.2020.101458.
[42] Bharat Mehta, et al., Microstructure , mechanical properties and fracture mechanisms in a 7017 aluminium alloy tailored for powder bed fusion - laser beam, Mater. Des. (ISSN: 0264-1275) 226 (2023) 111602, http://dx.doi.org/10.1016/j.matdes.2023.111602, URL https://doi.org/10.1016/j.matdes.2023.111602.
[43] Le Zhou, et al., Microstructure and tensile property of a novel AlZnMgScZr alloy additively manufactured by gas atomization and laser powder bed fusion, Scr. Mater. (ISSN: 13596462) 158 (2019) 24–28, http://dx.doi.org/10.1016/j.scriptamat.2018.08.025, URL https://doi.org/10.1016/j.scriptamat.2018.08.025.
[44] Zhiguang Zhu, et al., Selective laser melting of micron-sized niobium functionalized Al7075 alloy: Element evaporation and grain refinement, Mater. Sci. Eng. A (ISSN: 09215093) 834 (January) (2022) 142595, http://dx.doi.org/10.1016/j.msea.2022.142595, URL https://doi.org/10.1016/j.msea.2022.142595.
[45] Deqiao Xie, et al., Effect of higher laser power remelting on porosity and mechanical performance of part built by laser powder bed fusion, Int. J. Adv. Manuf. Technol. (ISSN: 1433-3015) 125 (February) (2023) 4779–4791, http://dx.doi.org/10.1007/s00170-023-11067-z, URL https://doi.org/10.1007/s00170-023-11067-z,
[46] Christian Weingarten, et al., Formation and reduction of hydrogen porosity during selective laser melting of AlSi10Mg, J. Mater. Process. Technol. (ISSN: 09240136) 221 (2015) 112–120, http://dx.doi.org/10.1016/j.jmatprotec.2015.02.013, URL http://dx.doi.org/10.1016/j.jmatprotec.2015.02.013.
[47] Mathieu Opprecht, et al., A solution to the hot cracking problem for aluminium alloys manufactured by laser beam melting, Acta Mater. (ISSN: 1359-6454) 197 (2020) 40–53, http://dx.doi.org/10.1016/j.actamat.2020.07.015, URL https://doi.org/10.1016/j.actamat.2020.07.015.
[48] Camille van der Rest, et al., Improving the fatigue life of laser powder bed fusion scalmalloy® by friction stir processing, Mater. Des. 244 (113193) (2024) http://dx.doi.org/10.1016/j.matdes.2024.113193, URL https://doi.org/10.1016/j.matdes.2024.113193.
[49] Maximilian Raab, Markus Bambach, Fatigue properties of scalmalloy® processed by laser powder bed fusion in as-built, chemically and conventionally machined surface condition, J. Mater. Process. Technol. (ISSN: 09240136) 311 (November 2022) (2023) http://dx.doi.org/10.1016/j.jmatprotec.2022.117811.
[50] S. Griffiths, et al., Effect of laser rescanning on the grain microstructure of a selective laser melted Al-Mg-Zr alloy, Mater. Charact. (ISSN: 10445803) 143 (March) (2018) 34–42, http://dx.doi.org/10.1016/j.matchar.2018.03.033.
[51] A.V. Gusarov, J.P. Kruth, Modelling of radiation transfer in metallic powders at laser treatment, Int. J. Heat Mass Transfer (ISSN: 00179310) 48 (16) (2005) 3423–3434, http://dx.doi.org/10.1016/j.ijheatmasstransfer.2005.01.044.
[52] C.D. Boley, et al., Metal powder absorptivity: modeling and experiment, Appl. Opt. (ISSN: 0003-6935) 55 (23) (2016) 6496, http://dx.doi.org/10.1364/ao.55.006496.
[53] Yusufu Ekubaru, et al., Excellent strength - ductility balance of Sc-Zr-modified Al-Mg alloy by tuning bimodal microstructure via hatch spacing in laser powder bed fusion, Mater. Des. (ISSN: 0264-1275) 221 (2022) 110976, http://dx.doi.org/10.1016/j.matdes.2022.110976, URL https://doi.org/10.1016/j.matdes.2022.110976.
[54] ANSYS Inc., Ansys GRANTA EduPack Software, Cambridge, UK, 2023.
[55] Fei Lv, et al., On the role of laser in situ re-melting into pore elimination of Ti e 6Al e 4V components fabricated by selective laser melting, J. Alloys Compd. (ISSN: 0925-8388) 854 (2021) 156866, http://dx.doi.org/10.1016/j.jallcom.2020.156866, URL https://doi.org/10.1016/j.jallcom.2020.156866.
[56] Charlotte de Formanoir, et al., Healing of keyhole porosity by means of defocused laser beam remelting: operando observation by X-ray imaging and acoustic emission-based detection, Addit. Manuf. (ISSN: 22148604) (2023) 103880, http://dx.doi.org/10.1016/j.addma.2023.103880, URL https://doi.org/10.1016/j.addma.2023.103880.